

## Arecibo Radar Mapping of the Lunar Poles: A Search for Ice Deposits

N. J. S. Stacy, D. B. Campbell,\* P. G. Ford

The Arecibo 12.6-centimeter wavelength radar system was used to image the polar regions of the moon at a resolution of 125 meters in a search for ice deposits in areas of possible permanent shadow from the sun. No areas greater than 1 square kilometer were found with high radar backscatter cross sections and high circular polarization ratios, properties suggestive of the presence of ice. A number of areas smaller than 1 square kilometer were found with these properties, but optical images from spacecraft missions have shown some of these features to be in sunlight. Arecibo radar images of Sinus Iridum at latitude 47°N also showed a number of small features with similar properties. The coincidence of some of these features with the radar-facing slopes of craters and their presence in sunlit areas suggests that very rough surfaces rather than ice deposits are responsible for their unusual radar properties.

Ground-based observations of the moon were conducted using the Arecibo Observatory, Puerto Rico, 2.38-GHz (12.6-cm wavelength) radar system to map regions of lunar surface radio-wave backscatter in two polarizations at high spatial resolution (1). Observations of the polar regions were further motivated by the ability of radar to image areas not illuminated by sunlight; such areas may provide an environment suitable for the preservation of ice deposits or other volatiles over geologic time scales (2). Here, we present ground-based radar images of the north and south lunar poles and analyze the polarization properties of the reflected signal in the context of the possible presence of ice.

It has been suggested that permanently shadowed regions of the lunar poles would have relatively constant surface and subsurface temperatures, possibly as low as 40 K, providing an environment suitable for the entrapment and storage of ices over geologic time scales (2). The discovery of anomalous radar backscatter from permanently shadowed crater floors near the poles of Mercury and the interpretation of these regions as areas of probable water ice deposits (3, 4) strengthened the possibility of finding similar deposits near the lunar poles. The interpretation that ice is responsible for the anomalous radar backscatter in the Mercury radar images rests primarily on the unusual radar backscatter characteristics of many icy surfaces in the solar system—that is, high backscatter cross section

per unit surface area ( $\sigma^0$ ) with a circular polarization ratio (CPR) greater than unity (5). Although ice, with a dielectric constant of 3.15, does not have an intrinsically high reflectivity, it has low loss and thus may serve as a weakly absorbing material containing a matrix of embedded scatterers; such a material could support volume-scattering mechanisms such as the coherent backscatter opposition effect (6). Recent bistatic radar observations of the lunar south pole by the Clementine spacecraft are reported to show a backscatter enhancement consistent with, but not unique to, the presence of ice deposits (7). In comparison, the backscatter characteristics of rock surfaces that are rough on the scale of the radar wavelength (such as lava flows) and are observed at high incidence angles generally include high backscatter cross sections and CPRs of  $\leq 1$  (8). However, CPRs greater than unity have been observed over rock surfaces. Areas of the blocky SP lava flow in northern Arizona observed at incidence angles of 42° to 52° have CPRs between 1 and 2.5 (9).

As viewed from the lunar poles, the Arecibo Observatory rises a maximum of  $\sim 6^\circ$  above the horizon [incidence angle of 84° (10)], but, given the 1.53° inclination of the moon's equatorial plane to the ecliptic plane, the limb of the sun can be up to 1.82° above the horizon. Because we lack detailed knowledge of the lunar topography, these small angles mean that an unknown fraction of the area shadowed from the sun is also shadowed from Arecibo and, hence, is not observable (for example, the floors of the large impact craters). At the lunar south pole, about 60% of the area below latitude 85°S is observed in the radar image, including much of the south pole area shown to be in solar shadow in Lunar Orbiter IV (11) and Clementine optical images (7, 12). However, areas shadowed in these space-

craft optical images are not necessarily in permanent shadow because of the 18.6-year precessional period of the lunar spin axis. The lack of detailed topographic information for the polar regions makes it impossible to determine which areas are in permanent shadow.

Radar images of the north and south polar regions of the moon were acquired in May and August 1992, respectively (1). A circularly polarized wave was transmitted from the main Arecibo antenna, and both senses of circular polarization—opposite circular (OC) and same circular (SC) (13)—were received at a smaller auxiliary antenna located 11 km from the Arecibo telescope. This bistatic radar arrangement permitted a pulsed radar experiment that avoided ambiguities in range (range aliasing) while maintaining an average data rate appropriate for the data acquisition hardware (14). The transmit signal was encoded with a pseudorandom code, and 16,384 pulses acquired in  $\sim 25$  min were combined to form a range-Doppler image with a resolution of  $\sim 125$  m and three or four looks (independent measurements of the backscatter from a given surface area). The final processing stage resampled the range-Doppler image into selenographic coordinates and applied small offsets to align the position of the poles with published locations (11).

The OC image of the north pole was acquired on 8 May 1992 when Arecibo was  $\sim 4.1^\circ$  above the horizon at the pole, resulting in extensive radar shadows from topographic features so that only  $\sim 40\%$  of the area above 85°N (28,900 km<sup>2</sup>) was imaged (Fig. 1A). The image shows a slight topographic high running from 85.5°N, 240°E to 85°N, 110°E, which appears to be caused by adjacent impact crater rims; this feature prevents the measurement of a radar echo from a large area in the lower half of the image. Most areas of enhanced backscatter are associated with surface slopes inclined toward the radar, such as the radar-facing slopes in highland areas and the radar-facing inner and outer walls of impact craters. Smooth plains such as the flooded floor of the impact crater Gioja (82.5°N, 1.2°W) and the adjacent impact basin centered at 84.5°N, 6°E are characterized by fairly uniform backscatter interrupted by numerous smaller impact craters. In comparison, the highland areas, such as the segment between 30°W and 55°W, 85°N to 90°N, have a hummocky appearance.

The south pole area was imaged on 18 August 1992 (Fig. 1B) when Arecibo was  $\sim 6.1^\circ$  above the horizon at the pole, so that  $\sim 60\%$  of the area below 85°S (43,300 km<sup>2</sup>) was imaged. Smooth plains are less prevalent in the south pole area, occurring main-

N. J. S. Stacy, Microwave Radar Division, Building 180L, Defence Science and Technology Organization, Post Office Box 1500, Salisbury, SA 5108, Australia.

D. B. Campbell, National Astronomy and Ionosphere Center and Department of Astronomy, Space Sciences Building, Cornell University, Ithaca, NY 14853, USA.

P. G. Ford, Center for Space Research, Massachusetts Institute of Technology, Cambridge, MA 02139, USA.

\*To whom correspondence should be addressed. E-mail: campbell@astrosun.tn.cornell.edu

ly in the floor of the crater Amundsen at 84.7°S, 82.2°E, in the area to the east of Amundsen around 85.7°S, 127.7°E, and in the region around 86.5°S, 75°W, which appears to be the floor of an impact feature centered at 85.5°S, 90°W in the Clementine optical image (7, 12).

The CPR images for the north and south pole regions have very similar characteristics. There are no extensive areas with CPRs approaching or greater than unity. The average CPRs for areas that appear to have little topographic expression (and are not in the radar shadow) are ~0.45 for the north pole and 0.37 for the south pole. If large craters and complex areas are included in these measurements, then the CPRs in-

crease to 0.54 and 0.45, respectively. These latter values are comparable to the ratio of 0.54 estimated from previous scattering law measurements for the average lunar surface at high incidence angles at 23-cm wavelength (15). The images of both poles show areas of high CPR associated with the radar-bright inner walls of several craters with rim diameters of <30 km as well as smaller radar-bright features, most of which appear to be associated with small craters. For these features, high SC backscatter cross sections correlate with the high CPRs, as shown in Fig. 2 for the south pole. For example, the large impact craters labeled A and B have radar-bright, radar-facing rims with CPRs near unity, whereas craters C and D have

less bright radar-facing rims with CPRs closer to the mean value. The relatively flat region around location E has a uniform CPR of 0.4. Backscatter values for the middle area of the radar-facing inner rim of the 20.5-km-diameter crater A, the south pole crater ( $\sigma_{oc}^o = 0.036$ , CPR =  $0.94 \pm 0.04$ ), are greater than the values for the left side (in the image) of the radar-facing inner rim of crater C ( $\sigma_{oc}^o = 0.001$ , CPR =  $0.38 \pm 0.02$ ). The top of the rim of crater A is illuminated by sunlight in the Lunar Orbiter IV and Clementine images (7, 11, 12), indicating that it is not in permanent shadow, which suggests that the presence of ice is not a viable explanation for the enhanced backscatter. Geometric effects such as double bounce may be responsible but hitherto have been clearly observed only when the surface geometry supports forward scatter into a second surface (1, 16). The most probable explanation is enhanced backscatter from increased wavelength-scale surface roughness in the rims of craters A and B. The enhanced backscatter areas are associated with steeper slopes; estimates of the inner rim slopes from the crater radar shadow are 37° above the horizontal for crater A and 20° for crater C.

Similar increases in the backscatter cross section and CPR for the radar-facing inner slopes of craters were measured in clearly sunlit areas of the moon away from the poles. Figure 3 shows the SC and CPR images for Sinus Iridum and the hummocky terrain to the northwest (centered on 47.2°N, 32.5°W). The two craters in the lower left of the images, with diameters of ~10 km, have CPRs in the range of 0.72 to 0.94 for several areas on the radar-facing rims. Histograms of the entire CPR images in Figs. 2B and 3B have similar mean values of 0.48 and 0.49, respectively, and the high CPR tails of both distributions extend past a CPR of 1.

A more puzzling problem than the near-

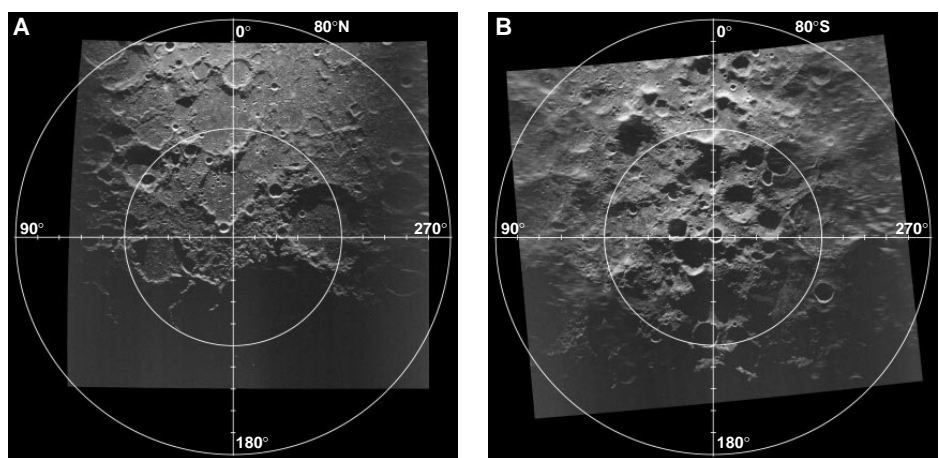
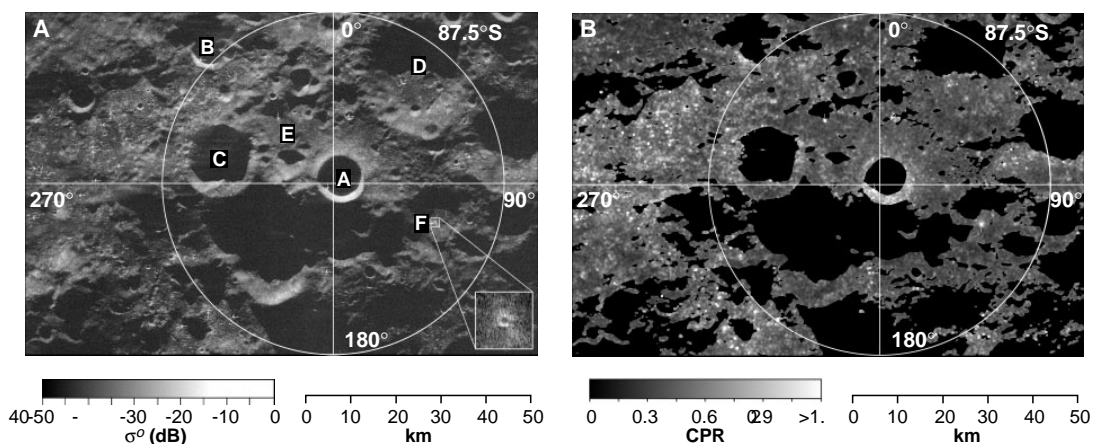


**Fig. 1.** OC backscatter image of (A) north pole and (B) south pole regions in a stereographic map projection. The radar signal incidence angle ( $\theta$ ) is 85.9° at the north pole and 83.9° at the south pole (4.1° and 6.1° above the local horizon, respectively). The incidence angle varies in proportion to latitude along approximately the 0° to 180° longitude line in these maps. The processed radar data were averaged to three looks with a resolution of 121 m in slant range (image top to bottom) for both images, 136 m in cross range (image left to right) for the north pole and 108 m in cross range for the south pole, before resampling to selenographic coordinates. The radar backscatter is shown in units of  $\sigma^o$ , in a logarithmic scale with an absolute error of ~3 dB (a factor of 2) (19). The sides of the south pole map show ghost images that were located at Doppler offsets beyond the radar sampling frequency (pulse repetition frequency) and were aliased into the processed Doppler bandwidth.

**Fig. 2.** Images of (A) the SC polarization backscatter and (B) the CPR of the south pole region. The SC image has three looks, and the ratio image was calculated from data averaged to 1-km resolution and ~230 looks using a boxcar filter, masked by the regions of radar shadow. Small radar-bright features with CPRs greater than unity are indicated by arrows. One of these features with extreme backscatter values is the 840-m-diameter impact crater at 88.4°N, 110°E, labeled F. The single-look image with a resolution of 121 m in range by 36 m in cross range (inset in A) shows that the radar-bright area is associated with the crater rim.



unity CPRs for the slopes of some of the larger craters is the problem of CPRs greater than unity for (i) a number of craters with diameters of <1 km, (ii) small features that are probably craters with sizes near or below the image resolution, and (iii) regions of <1 km<sup>2</sup> on the radar-facing slopes of some of the larger craters. Twenty-six of these features were identified in the region of the south pole shown in Fig. 2. The CPRs for these features varied from ~1.2, a lower limit set by a selection requirement that the average CPR be  $\geq 2$  standard deviations above unity, to 2.6 (17, 18). Their SC backscatter cross sections varied from 0.022 to 0.002. If the same expression as in Harmon *et al.* (4) is used to correct for the incidence angle, these cross sections correspond to full-disk albedos in the range 0.7 to 0.06, with half the features having a value close to 0.1. This range is similar to that obtained by Harmon *et al.* for the possible polar ice deposits on Mercury, although the median value is somewhat lower and the sizes of the regions are much smaller than those found on Mercury. However, examination of a mosaic of the south pole region made from Clementine images (12) indicates that at least 9 of the 26 features, primarily those in the smooth plains area to the left of crater C in Fig. 2 (near 86.5°S, 75°W), are in sunlit areas. This estimate is probably low because the Clementine images were obtained in the lunar southern winter, when the lunar spin axis was tilted so that the south pole pointed away from the sun (7); more of these features are likely to be in sunlight during the course of the lunar year and during the 18.6-year precessional period of the lunar spin axis.

An examination of the north pole and Sinus Iridum regions found a comparable number of small regions with high cross

sections and CPRs of 1.2 to 2.2. Many of the features in the Sinus Iridum area are associated with the steep impact basin walls, but some are also associated with small craters. Consequently, scattering mechanisms associated with a high degree of wavelength-scale surface roughness (9) seem the most probable explanation for the high  $\sigma^0$ 's and CPRs of these small features. These same properties may, of course, also be indicative of ice for those features in permanent shadow. Feature F in Fig. 2A has a CPR of  $2.4 \pm 0.14$  and an SC cross section of 0.022 for an area of 0.42 km<sup>2</sup>, and is the best candidate in the Arecibo data for a reflection from ice. However, as can be seen from the subimage of feature F in Fig. 2A, the high SC backscatter is from the radar-facing outer and inner slopes of the crater's walls. It is not clear why this would be the case if the high radar return were the result of volume scattering in ice on the crater floor. This association of the enhanced scatter with the crater walls again suggests that a rough-surface scattering mechanism may be responsible.

The similarities in the Arecibo and Clementine bistatic radar (7) experiments make them suitable for comparison. Both used a 2.38-GHz radar system and measured the scattered circular polarization signal. Although the transmitter positions were different, both used a ground-based receiver, and thus the collected signal was constrained by the Earth-moon geometry. The Arecibo image of the south pole area, acquired with the Arecibo telescope 6.1° above the horizon, imaged fractionally more features within the south pole region than did Clementine, where the receiving antenna was 4.5° to 5.5° above the horizon. Shadows evident in Fig. 2A clearly show that the geometry for both the Arecibo and Clementine experiments

**Table 1.** Arecibo and Clementine CPR measurements.

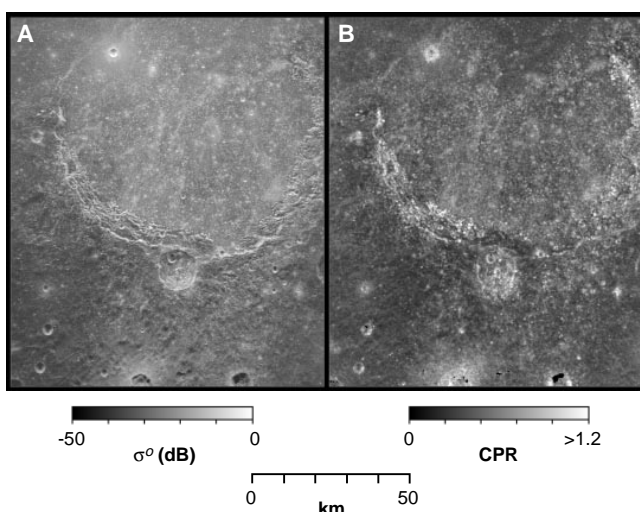
Region	Clem-entine footprint area (km <sup>2</sup> )	Clem-entine CPR	Arecibo CPR
South pole	45,000	0.45	0.51
Near south pole	170,000	0.29	0.43*
North pole	45,000	0.35	0.50

\*The Arecibo measurement is the central 87,000 km<sup>2</sup> of the Clementine footprint.

precluded measurement of radar scatter from the floors of the craters at the south pole. Maps of the Clementine south pole footprints (7) and our best understanding of the north pole footprint were used to crop the Arecibo data and calculate CPRs for comparison with the Clementine measurements. The Arecibo results, which show similar CPRs for the two poles, do not agree with the Clementine measurement that showed a significantly enhanced CPR for the south pole relative to the north pole and to a reference area near the south pole (Table 1). The Clementine experiment measured the radar cross sections as a function of the bistatic angle  $\beta$  for a large area (per observation), whereas the Arecibo experiment measured the backscatter signal ( $\beta = 0$ ) at high spatial resolution. The Clementine data show a CPR enhancement near  $\beta = 0$ , whereas the Arecibo data show only small (<1 km<sup>2</sup>) areas with CPR > 1. If the enhancement in the south pole CPR measured by Clementine around  $\beta = 0$  is attributable to the high-CPR areas identified in the much finer resolution Arecibo data set, then, because these areas are typically associated with impact craters and some appear to be in sunlit areas, the observed phenomena may be attributable to rough-surface scattering.

Because of the association of the high CPR areas with impact features and the location of many of these areas in sunlit regions, there is no clear evidence from the Arecibo images for the presence of ice. Most high CPR areas appear to be the result of increased surface roughness or blocky areas associated with the steep inner rim slopes of impact craters.

**Fig. 3.** Images of (A) the SC polarization backscatter and (B) the CPR of Sinus Iridum and the area to the northwest (centered on 47.2°N, 32.5°W) in the radar delay-Doppler projection. The images are 360 km high by 340 km wide, are oriented with southeast to the top and northwest to the bottom, and have an incidence angle varying from 52.4° at the top to 64.0° at the bottom. The ratio image was calculated from data averaged to ~1.5-km resolution with 256 looks. The inner slopes of the three craters at the lower left, the ejecta of the medium-size crater at the upper middle left, and many areas around the basin rim have CPRs around unity.



REFERENCES AND NOTES

1. N. J. S. Stacy, thesis, Cornell University (1993).
2. K. Watson, B. C. Murray, H. Brown, *J. Geophys. Res.* **66**, 3033 (1961); J. R. Arnold, *ibid.* **84**, 5659 (1979); J. D. Burke, in *Lunar Bases and Space Activities of the 21st Century*, W. W. Mendell, Ed. (Lunar and Planetary Institute, Houston, TX, 1985), pp. 77–84.
3. M. A. Slade, B. J. Butler, D. O. Muhleman, *Science* **258**, 635 (1992); J. K. Harmon and M. A. Slade, *ibid.*, p. 640.
4. J. K. Harmon *et al.*, *Nature* **369**, 213 (1994).
5. D. B. Campbell, J. F. Chandler, S. J. Ostro, G. H. Pettengill, I. I. Shapiro, *Icarus* **34**, 254 (1978); D. O. Muhleman, B. J. Butler, A. W. Grossman, M. A.

- Slade, *Science* **253**, 1508 (1991).
6. B. Hapke, *Icarus* **88**, 407 (1990).
  7. S. Nozette *et al.*, *Science* **274**, 1495 (1996);
  8. B. A. Campbell and D. B. Campbell, *J. Geophys. Res.* **97**, 16293 (1992), figure 9 and table 6; J. K. Harmon and S. J. Ostro, *Icarus* **62**, 110 (1985).
  9. B. A. Campbell, R. E. Arvidson, M. K. Shepard, *J. Geophys. Res.* **98**, 17099 (1993), figure 11.
  10. The incidence angle is the angle between the incident radiation and the local vertical (mean surface normal). Near the lunar poles, the incidence angle for Earth-based observations approaches 90°. An imaging radar system forms a map of the surface backscatter from range-Doppler measurements of backscatter. The projection of range-Doppler coordinates onto a surface at high incidence angles is similar to a regular grid in surface coordinates, resulting in a "plan view" of the surface backscatter.
  11. G. L. Gutschewski, D. C. Kinsler, E. Whitaker, *Atlas and Gazetteer of the Near Side of the Moon* (NASA, Washington, DC, 1971).
  12. E. M. Shoemaker, M. S. Robinson, E. M. Eliason, *Science* **266**, 1851 (1994).
  13. The two senses of circular received polarizations contain the OC and SC components of the backscatter signal. The OC component is the circular polarization sense expected from a single reflection with a plane interface, and the SC component is the orthogonal circular polarization. The main contributions to the backscatter signal are from single quasi-specular reflections (caused by mirrorlike reflection from smooth facets possibly many wavelengths in size) and diffuse scattering mechanisms (arising from wavelength-size surface and near-surface structures). These effects contribute to the OC signal and to both received polarizations, respectively. Backscatter from two successive quasi-specular reflections is not expected to contribute appreciably to the SC signal because of the low intrinsic reflectivity of the lunar surface.
  14. In a pulsed-radar experiment, a short burst of energy is transmitted and the echo is received during the transmitter off time. The fraction of the time spent transmitting (the duty cycle) varied from 2% to 15% for our lunar observations.
  15. T. Hagfors, *Radio Sci.* **5**, 189 (1970).
  16. Double-bounce scattering has been identified in radar observations of the crater Carlini (33.7°N, 24.0°W) in Mare Imbrium where forward scatter from the front inner rim is reflected a second time from the radar-facing inner rim (1), and in observations of terrace structures in the rim of the crater Copernicus.
  17. The multi-look OC and SC image pixel values are random variables with  $\chi^2$  distributions and  $2N$  degrees of freedom, where  $N$  is the number of independent looks. Assuming that the OC and SC random variables are independent and the local surface is homogeneous (so measurements from adjacent pixels used in the averaging are from the same distribution), the CPR follows an F distribution with  $2N$  degrees of freedom. For large  $N$  (for example,  $>25$ ), the fractional SD of the F distribution is given by approximately  $(2/N)^{1/2}$ .
  18. Small features with high CPRs were identified as regions of adjacent pixels (in the up-down and left-right directions, not at 45°) with CPRs  $> 1.2$  from the four-look data. If such a region was found to contain 10 or more pixels, then it was encompassed by a rectangle and the mean OC and SC backscatter of all the pixels within the rectangle and above a signal-to-noise ratio threshold were calculated (a threshold of 15 dB for the OC polarization was used for the south pole data analysis). The CPR for the region was calculated from the ratio of the rectangle mean SC and OC backscatter values. If the cumulative F distribution for the region polarization ratio had a value greater than 0.9773, then the region was accepted as a candidate high-CPR feature. (The cumulative F distribution was used here to test whether a CPR was significantly different from a value of 1.)
  19. Most of the absolute backscatter uncertainty is attributable to systematic errors, which apply equally to both the SC and OC cross-section measurements. Consequently, the uncertainty in the CPR (= SC/OC)

is almost entirely attributable to the statistical uncertainties in the SC and OC cross sections.

20. We thank P. Perillat, A. Crespo, A. Hine, and other support staff at the Arecibo Observatory who helped to make these lunar observations possible. Supported in part by NASA grant NAGW 3985 from the Plan-

etary Geology and Geophysics program. The National Astronomy and Ionosphere Center is operated by Cornell University under a cooperative agreement with NSF, and is also supported by NASA.

6 February 1997; accepted 23 April 1997

## The Source of Green Light Emission Determined from a Heavy-Ion Storage Ring Experiment

D. Kella, L. Vejby-Christensen, P. J. Johnson, H. B. Pedersen, L. H. Andersen\*

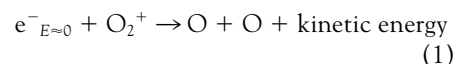
The final electronic states of oxygen atoms formed by dissociative recombination of  $O_2^+$  with cold electrons have been measured by an imaging technique at a heavy-ion storage ring. The  $^3P$ ,  $^1D$ , and  $^1S$  quantum yield for  $O_2^+$  in the vibrational ground level was found to be 0.86, 1.09, and 0.05, respectively. The yield of the  $^1S$  state, which is responsible for the 5577 angstrom green light from upper planetary atmospheres, was more than an order of magnitude larger than the theoretical value used in atmospheric models. The results may help refine the models of the chemistry and dynamics of the ionosphere and provide guidance for further quantum-chemistry calculations.

During the daytime, the atmosphere is exposed to ultraviolet sunlight that creates ionized molecules like  $O_2^+$ . At nighttime, the molecular ions may recombine with electrons and dissociate into atomic fragments with electronic excitation. The subsequent emission of light from excited atoms in the atmosphere gives rise to several characteristic lines in the emission spectrum. The green line at 5577 Å, which is a prominent feature of the spectrum of the night sky, was detected more than 100 years ago by Campbell (1). In 1927 McLennan and co-workers suggested that the origin of this line is the forbidden transition in atomic oxygen  $^1S \rightarrow ^1D$  (2). A few years later Kaplan (3) suggested that the excited  $O(^1S)$  atoms might be a product of dissociative recombination (DR), and in 1947 Bates and Massey (4) pointed out that DR of  $O_2^+$  was indeed the only process that could explain the observed electron recombination rates in the ionosphere of Earth ( $\geq 100$ -km altitude).

Knowledge of the rate of production of O atoms in different electronic states is important for aeronomers who extensively use the 5577 Å  $O(^1S)$  green line emission as a source of information about the chemistry and dynamics of the ionosphere (5, 6). Despite many years of experimental and theoretical research, the distribution of specific excited states of atomic oxygen as a result of DR is still uncertain. The interpretation of laboratory as well as observational data has

been difficult and controversial due to the lack of such knowledge. For example, the expectation of a very low fraction of oxygen atoms in the  $^1S$  excited state has led to speculation that an unknown source of  $O(^1S)$  might exist in the atmosphere, or the  $O_2^+$  ions might have an unusually high degree of vibrational excitation that causes an enhanced  $^1S$  yield (7, 8). Molecular oxygen ions are abundant in the atmosphere of Earth as well as in the atmospheres of other planets like Mars and Venus. Because DR provides neutral oxygen atoms with a kinetic energy that depends on their final electronic states, the branching ratios for formation of oxygen in the various electronic states are needed to model the heating of such atmospheres as well as for determining the continuous escape of atoms from the atmospheres (9, 10).

The DR of  $O_2^+$  with low-energy electrons ( $E \approx 0$ ) may be written as



It involves transformation of potential and kinetic energy from the incoming electron,  $e^-$ , into electronic excitation and kinetic energy of the atoms after dissociation of the molecule. To understand the direct DR process, in which the electron is captured into a doubly excited repulsive electronic state, knowledge about the initial potential-energy curve of the molecular ion, the repulsive curves of the excited, neutral molecule, and the capture probability of the relevant curves is required. In addition, the progression along the repulsive curves, often with

Institute of Physics and Astronomy, University of Aarhus, DK 8000, Aarhus C, Denmark.

\*To whom correspondence should be addressed. E-mail: lha@dfi.aau.dk